



Catalytic behavior of supported Ru nanoparticles on the {100}, {110}, and {111} facet of CeO₂



Fei Wang, Changming Li, Xiaoyu Zhang, Min Wei*, David G. Evans, Xue Duan

State Key Laboratory of Chemical Resource Engineering, Beijing University of Chemical Technology, Beijing 100029, PR China

ARTICLE INFO

Article history:

Received 17 July 2014

Revised 24 March 2015

Accepted 18 May 2015

Keywords:

Ru/CeO₂ catalysts

CO₂ methanation reaction

Oxygen vacancy

Morphology dependence

Metal–support interaction

ABSTRACT

The existence of oxygen vacancies in heterogeneous catalysis plays an essential role in determining the catalytic reactivity of metal catalysts. In this work, Ru nanoparticles were immobilized onto the CeO₂ nanocubes (NCs), nanorods (NRs), and nanopolyhedrons (NPs) with the dominantly exposed {100}, {110}, and {111} facet of CeO₂ support, respectively. Their catalytic behavior toward CO₂ methanation was studied in detail, and the highest catalytic rate per gram of catalyst was obtained over the Ru(3%)/CeO₂-NCs catalyst (reaction rate: 4.85×10^{-8} mol g_{cat}⁻¹ s⁻¹; selectivity: 99%; 150 °C). The temperature-programmed reduction (TPR), Raman spectra, and oxygen storage capacity (OSC) test confirm that the Ru(3%)/CeO₂-NCs catalyst possesses the highest concentration of oxygen vacancies owing to the Ru-promoted formation of oxygen vacancy on the CeO₂-NCs. In addition, *in situ* infrared spectroscopy measurements demonstrate that the abundant oxygen vacancy in Ru(3%)/CeO₂-NCs serves as the active site for CO₂ activation, accounting for the significantly enhanced low-temperature reaction rate per gram of Ru/CeO₂ catalyst.

© 2015 Elsevier Inc. All rights reserved.

1. Introduction

CeO₂, a well-known functional rare earth material, has been extensively used in a variety of applications, including catalysis [1–3], ultraviolet blocking/shielding materials [4,5], fuel cells [6,7], and oxygen sensors [8]. Specially, their unique oxygen storage capacity resulting from the rich oxygen vacancies in CeO₂ has attracted considerable research interest in catalytic oxidation reactions (e.g., CO oxidation [9–14], CO₂ reforming of methane [15–17], catalytic combustion of chlorobenzene [18,19]). Recent studies reported that the oxygen vacancies are highly relevant to the morphology of CeO₂, and great efforts have been made for shape-controlled synthesis of CeO₂ to enrich the surface oxygen vacancies concentration for better performance [20–27]. Although great process has been made for CeO₂-based catalysts in oxidation reactions, the effects of oxygen vacancies on hydrogenation reaction process are rarely discussed. Indeed, except crystal face effect, the reducing atmosphere (e.g., H₂) can also induce the generation of oxygen vacancies [1], which may have great impact on the activation of oxygen-containing reactants (e.g., CO, CO₂) during their hydrogenation process. The deep insight into the influence of oxygen vacancies on hydrogenation reactions

would further expand the design and application of CeO₂ as excellent catalysts.

The methanation of CO₂ is an important catalytic process to recycle CO₂ emissions to give a useful fuel with potential commercial applications and environmental benefits [28]. Hydrogenation of CO₂ at low temperature is always difficult because the reduction of fully oxidized carbon to methane is an eight-electron process with significant kinetic limitations [29,30]. This means that the catalytic reaction has to be operated at a high temperature with an energy-waste process. Early studies found the loading of small metal nanoparticles on the reducible supports (e.g., TiO₂, CeO₂) can significantly enhance their methanation performance owing to the metal–support interactions [31–37]. Some reports even speculated that the oxygen vacancies from the support may participate in the activation of inert CO₂ such as in the Ni/CeO₂ and Rh/TiO₂ systems [33,37]. However, owing to the restriction of synthetic routes and characterization methods in that stage, a detailed understanding on the effects of oxygen vacancies may be impossible. Recent developments in a sophisticated synthetic strategy and advanced characterization technique for oxygen vacancies provide new chance to this conundrum, which inspires us to tune the oxygen vacancies in metal/CeO₂ catalysts so as to disclose the relationship between the oxygen vacancy concentration and catalytic behavior.

Herein, we demonstrate the facile fabrication of Ru/CeO₂ catalysts by employing CeO₂ nanocubes (NCs), nanorods (NRs), and

* Corresponding author. Fax: +86 10 64425385.

E-mail address: weimin@mail.buct.edu.cn (M. Wei).

nanopolyhedrons (NPs) as the support (denoted as Ru/CeO₂-NCs, Ru/CeO₂-NRs, and Ru/CeO₂-NPs, with the dominantly exposed {100}, {110}, and {111} facet of CeO₂ support, respectively), which exhibit significant support-morphology-dependent catalytic activity toward CO₂ methanation. Specially, the Ru(3%)/CeO₂-NCs sample shows extraordinarily high catalytic rate per gram of catalyst at low temperature, with a reaction rate of 4.85×10^{-8} mol g_{cat}⁻¹ s⁻¹ at as low as 150 °C. The TPR, Raman spectra, and OSC confirm that the Ru(3%)/CeO₂-NCs catalyst possesses the highest concentration of oxygen vacancies, as a result of the Ru-promoted formation of oxygen vacancies on the {100} facet of CeO₂. Moreover, *in situ* infrared spectroscopy reveals that the abundant oxygen vacancies at the interface of Ru and CeO₂-NCs facilitate the CO₂ activation, accounting for its significantly enhanced low-temperature activity. Therefore, this work provides an effective method for the preparation of supported Ru catalysts by modulating the morphology and surface property of CeO₂ support, which can be potentially used in carbon recycle.

2. Experimental section

2.1. Materials

Chemical reagents, including Ce(NO₃)₃·6H₂O and RuCl₃·3H₂O, was purchased from Sigma–Aldrich. Deionized water was used in all the experimental processes.

2.2. Preparation of CeO₂

CeO₂ materials with various morphologies were synthesized by a hydrothermal method similar to the previous report [38]. For the preparation of CeO₂-NCs, a NaOH solution (14 M, 30 mL) was added dropwise into a Ce(NO₃)₃ solution (0.113 M, 40 mL) under stirring at room temperature, followed by an additional stirring for 30 min with the formation of a milky slurry. The mixture was transferred into a 100-mL stainless steel autoclave, tightly sealed and hydrothermally treated at 180 °C for 24 h. The resulting precipitate was collected, washed thoroughly, and dried at 60 °C for 12 h, followed by a calcination process in a muffle oven at 500 °C for 4 h to obtain the final CeO₂-NCs. The synthesis procedure for CeO₂-NRs and CeO₂-NPs was the same as that for CeO₂-NCs except that the hydrothermal treatment temperature was 100 °C and the concentration of NaOH solution was 0.275 M, respectively.

2.3. Preparation of Ru/CeO₂ catalyst

The Ru(3%)/CeO₂-NCs catalyst with a Ru loading of 3 wt% was prepared by the precipitation deposition method. Firstly, 3.0 g of CeO₂-NCs was suspended in 80 mL of water followed by adding 0.22 g of RuCl₃·3H₂O. The suspension pH was adjusted to 8.0 with NH₃·H₂O aqueous solution (0.1 M), and the resulting suspension was aged at room temperature for 3 h with stirring. The precipitation obtained was separated by centrifugation, washed thoroughly, and dried at 60 °C for 12 h, followed by calcination in air at 500 °C for 4 h. The obtained sample was denoted as RuO₂(3%)/CeO₂-NCs. Samples with different CeO₂ morphologies (NRs and NPs) and Ru loadings (1 wt%, 6 wt%, and 13 wt%) were also prepared by a similar method and were denoted as RuO₂(3%)/CeO₂-NRs, RuO₂(3%)/CeO₂-NPs, RuO₂(1%)/CeO₂-NCs, RuO₂(6%)/CeO₂-NCs, and RuO₂(13%)/CeO₂-NCs, respectively. Finally, all of the as-calcined RuO₂/CeO₂ samples were reduced in a gaseous mixture of H₂ and N₂ (2:3, v/v) for 4 h at 400 °C with a heating rate of 5 °C min⁻¹, and the resulting catalysts were denoted as Ru(3%)/CeO₂-NCs, Ru(3%)/CeO₂-NRs, Ru(3%)/CeO₂-NPs, Ru(1%)/CeO₂-NCs, Ru(6%)/CeO₂-NCs, and Ru(13%)/CeO₂-NCs, respectively.

2.4. Catalyst characterization

Transmission electron microscopy (TEM) and high-resolution TEM (HRTEM) observations were carried out on a JEOL JEM-2100 transmission electron microscope. The average particle diameter of Ru (d_{TEM}) was obtained by using the TEM results based on the following correlation:

$$d_{\text{TEM}} = \frac{\sum_i n_i d_i}{\sum_i n_i} \quad (1)$$

where d_i is the particle diameter measured by TEM and n_i is the particle number. X-ray diffraction (XRD) patterns of samples were obtained on a Shimadzu XRD-6000 diffractometer, using Cu K α radiation ($\lambda = 0.154$ nm) at 40 kV, 30 mA, a scanning rate of 5° min⁻¹, a step size of 0.02° s⁻¹, and a 2 θ angle ranging from 20° to 70°. Elemental analysis of metal in samples was performed using a Shimadzu ICPS-7500 inductively coupled plasma emission spectrometer (ICP-AES). Low-temperature N₂ adsorption–desorption isotherms of the samples were obtained on a Micromeritics ASAP 2020 sorptometer apparatus. All samples were outgassed prior to analysis at 200 °C for 12 h under 10⁻⁴ Pa vacuum. The total specific surface area was evaluated from the multipoint Brunauer–Emmett–Teller (BET) method. The extended X-ray absorption fine structure (EXAFS) spectroscopy of the samples was performed at the beam line 1W1B of the Beijing Synchrotron Radiation Facility (BSRF), Institute of High Energy Physics (IHEP), Chinese Academy of Sciences (CAS). The typical energy of the storage ring was 2.5 GeV with a maximum current of 250 mA. The Si (1 1 1) double-crystal monochromator was used. Fourier transform of the EXAFS spectra was carried out in a K-range from 3.0 to 12.8 Å⁻¹. The IFFEFIT 1.2.11 data analysis package (Athena, Artemis, Atoms, and FEFF6) was used for the data analysis and fitting. X-ray photoelectron spectroscopy (XPS) measurements were performed using an ESCALAB 250 instrument (Thermo Electron) with Al K α radiation. The binding energy calibration of all spectra was referenced to the C1s signal at 284.6 eV. Positron annihilation measurements were performed with a fast–slow coincidence ORTEC system with a time resolution of 187 ps for the full width at half maximum. A 5 × 10⁵ Bq source of ²²Na was sandwiched between two identical samples. The steady-state isotope transient kinetic analysis (SSITKA)-type *in situ* DRIFT infrared spectroscopy was recorded using a Vertex 70 (Bruker) spectrophotometer at 150 °C with 4 cm⁻¹ of resolution. Temperature-programmed reduction (TPR) and temperature-programmed desorption (TPD) of the samples were performed by using a Micromeritics ChemiSorb 2720 with a thermal conductivity detector (TCD). Before measurement, the sample (100 mg) placed in a quartz U-tube reactor was degassed under flowing argon at 200 °C for 2 h. For TPR, the sample was reduced in a stream of H₂/Ar (1:9, v/v; 40 mL min⁻¹ total flow) with a heating rate of 10 °C min⁻¹ up to 900 °C. For the H₂-TPD process, the sample (100 mg) was first sealed and reduced in the reactor in the gaseous mixture of H₂ and Ar (1:9, v/v) at 400 °C for 3 h. Subsequently, the reduced sample was purged in Ar at 500 °C for 30 min to remove excess hydrogen and then cooled down to 25 °C for re-adsorption of H₂; finally, a stream of argon (40 mL min⁻¹) was introduced to perform the TPD measurement with a temperature ramp of 10 °C min⁻¹. The dispersion of Ru was calculated based on the volume of chemisorbed H₂ using the following simplified equation:

$$D (\%) = \frac{2 \times V_{\text{ad}} \times M_{\text{metal}} \times SF}{m \times P \times V_m \times d_r} \times 100 \quad (2)$$

where m denotes the weight of sample (g); P is the weight fraction of Ru in the sample as determined by ICP; V_m is the molar volume of H₂ (22414 mL mol⁻¹) at standard temperature and pressure (STP); d_r is the reduction degree of Ru; V_{ad} (mL) is the volume of

chemisorbed H₂ at STP measured in the TPD procedure; M_{metal} is the molecular weight of Ru (101.07 g mol⁻¹); and SF is the stoichiometric factor (Ru:H molar ratio in the chemisorption) which is taken as 1. The average particle diameter ($d_{\text{dispersion}}$) based on metal dispersion was calculated assuming hemispherical particles by using the following equation:

$$d_{\text{dispersion}} = \frac{6A_W\sigma}{\rho_{\text{Ru}}N_A D} \quad (3)$$

where A_W is the atomic weight; σ is the areal surface atom density (1.58×10^{15} atoms cm⁻²); ρ_{Ru} is the density of Ru (12.45 g cm⁻³); and N_A is the Avogadro's number.

In order to quantitatively determine the concentration of surface oxygen vacancies in these CeO₂ samples, the oxygen storage capacity (OSC) measurements were carried out by the oxygen pulse injection method. Before analysis, the sample (200 mg) was reduced by H₂/Ar (1:9, v/v; 40 mL min⁻¹ total flow) at 400 °C for 2 h. Since the CO₂ activation by oxygen vacancy only occurs at the CeO₂ surface, the surface oxygen vacancy was measured. For this reason, the catalyst was cooled to room temperature (25 °C) under Ar flow (40 mL min⁻¹), and a stream of O₂/He (1:9, v/v; 40 mL min⁻¹ total flow) was periodically injected into the reduced sample until saturation. The consumption of oxygen was accordingly calculated and defined as OSC_{catalyst}. The consumption of oxygen by Ru is defined as OSC_{metal} which is calculated by the following equation:

$$\text{OSC}_{\text{metal}} = \frac{Dw_{\text{metal}}}{M_{\text{metal}}} \quad (4)$$

where D is the metal dispersion (%); w_{metal} is the wt% of metal, and M_{metal} is the molar weight of the metal; the stoichiometric factor between metal atom and oxygen atom is set as 1:1. The experimental value of surface oxygen vacancy concentration is defined as OSC_{surface-e} and calculated by the following equation:

$$\text{OSC}_{\text{surface-e}} = \text{OSC}_{\text{catalyst}} - \text{OSC}_{\text{metal}} \quad (5)$$

In order to examine the rationality of the experimental determination for OSC_{surface-e}, the theoretical maximum of surface oxygen vacancy concentration (OSC_{surface-t}) was also obtained according to the crystal institutions by the following equation:

$$\text{OSC}_{\text{surface-t}} = \frac{nS}{Nab} \quad (6)$$

where S is the BET surface area (m² g⁻¹); n is the fraction of reducible O in the unit cell; N is the Avogadro number, and a , b are the lattice parameter of support. This calculation is based on the following assumptions:

- (i) All the Ce⁴⁺ in the surface monolayer are reduced to the oxidation state +3.
- (ii) The CeO₂-NCs expose 100% of {100} facet; the CeO₂-NRs expose 50% of {110} facet and 50% of {100} facet [22]; the CeO₂-NPs expose 98% of {111} facet and 2% of {100} facet estimated by the TEM results.
- (iii) The {100} facet contains 2 Ce atoms and 4 O atoms per unit surface area ab ($a = b = 5.41$ Å); the {110} facet contains 2 Ce atoms and 4 O atoms per unit surface area ab ($a = 5.41$ Å, $b = 3.83$ Å); the {111} facet contains 2 Ce atoms and 4 O atoms per unit surface area ab ($a = 6.63$ Å, $b = 3.83$ Å).

2.5. Evaluation of catalytic performance

The catalytic evaluation of the supported Ru catalysts for CO₂ methanation was carried out in a quartz tube reactor (8 mm in diameter) at atmospheric pressure. Brooks mass-flow controllers were used to control the gas flow rate. In order to eliminate the

temperature and concentration gradient, 1.0 g of the catalyst was mixed with 1 mL of inert quartz sand (40–60 mesh; density: ~1.27 g/mL) and then packed into the reactor. The reactor temperature was controlled by three thermocouples (located near the entrance, at the middle, and near the exit of the bed). After the catalyst pretreatment (see details in Section 2.3), the reaction gas mixture consisting of CO₂ (15%, v/v), H₂ (60%, v/v), and Ar (25%, v/v) at 40 standard cubic centimeters per minute (sccm) total flow rate was introduced into the reactor, and the CO₂ conversion was measured over the temperature range 100–300 °C. The product gas stream was analyzed on line by gas chromatography (GC, Shimadzu, 2014C) equipped with a thermal conductivity detector (H₂, CO and CO₂) and a flame ionization detector (CH₄). The condensate was also analyzed by gas chromatography–mass spectrometry (GC–MS) off line.

Due to the high selectivity toward CH₄ (>99%) in this reaction, the reaction rate (r) was defined as the mole number of CH₄ produced per total mass of catalyst per second. The turnover frequency with respect to Ru (TOF_{Ru}) was defined as the number of CH₄ molecules produced per surface Ru atom per second. The number of surface Ru atom was obtained by the dispersion data. The turnover frequency with respect to oxygen vacancy concentration (TOF_{oxygen vacancy}) was defined as the number of CH₄ molecules produced per surface oxygen vacancy calculated by the OSC test. Activity measurements were performed at a low CO₂ conversion (<10%) in order to ensure that the reaction occurred in the kinetic region (Fig. S1). To compare the CO₂ methanation activity over the Ru/CeO₂ catalyst, apparent activation energy (E_a) was calculated in addition to TOF. The rate of CH₄ formation (r) was measured as a function of temperature (T) in the range 100–150 °C. Arrhenius plot ($\ln r$ vs. T^{-1}) is obtained, and the slope is used to calculate E_a by using the following equation:

$$E_a = -R \frac{d \ln r}{d(1/T)} \quad (7)$$

3. Results and discussion

3.1. Structural and morphological study

TEM was performed to probe the crystallite growth and structure of the three CeO₂ samples with different morphology. Fig. 1A₁ shows the uniform cube morphology of CeO₂-NCs with a side size of approximately 20–30 nm. The high-resolution TEM (HRTEM) image in Fig. 1B₁ displays clear {200} lattice fringes with an interplanar spacing of 0.27 nm, indicating that CeO₂-NCs selectively expose the {100} planes, as shown in the schematic diagram (Fig. 1C₁). For the rod-like CeO₂ (CeO₂-NRs) in Fig. 1A₂, they have a uniform diameter of ~10 nm with the length in the range 50–200 nm. An interplane spacing of 0.19 nm attributed to the {220} planes was observed (Fig. 1B₂), indicating CeO₂-NRs show a preferred 1D growth direction along [110], and thus are enclosed by {110} and {100} planes (Fig. 1C₂). The polyhedron shape CeO₂ sample (CeO₂-NPs) was also synthesized with a uniform particle size of 10–15 nm as shown in Fig. 1A₃. The corresponding HRTEM image (Fig. 1B₃) displays clear {111} and {200} lattice fringes with the interplanar spacing of 0.31 and 0.27 nm, respectively, revealing that CeO₂-NPs are dominated by a truncated octahedral shape enclosed by the {111} and {100} facet (Fig. 1C₃). In conclusion, only {100} facet exists in the CeO₂-NCs, while {110} and {111} facet are the mainly exposed planes for CeO₂-NRs and CeO₂-NPs, respectively.

Fig. 2 illustrates the XRD patterns of the three CeO₂ samples with different morphology (Fig. 2a–c) and the corresponding supported Ru samples (Ru(3%)/CeO₂, Fig. 2d–f). It can be found that the CeO₂-NCs (Fig. 2a), CeO₂-NRs (Fig. 2b), and CeO₂-NPs (Fig. 2c)

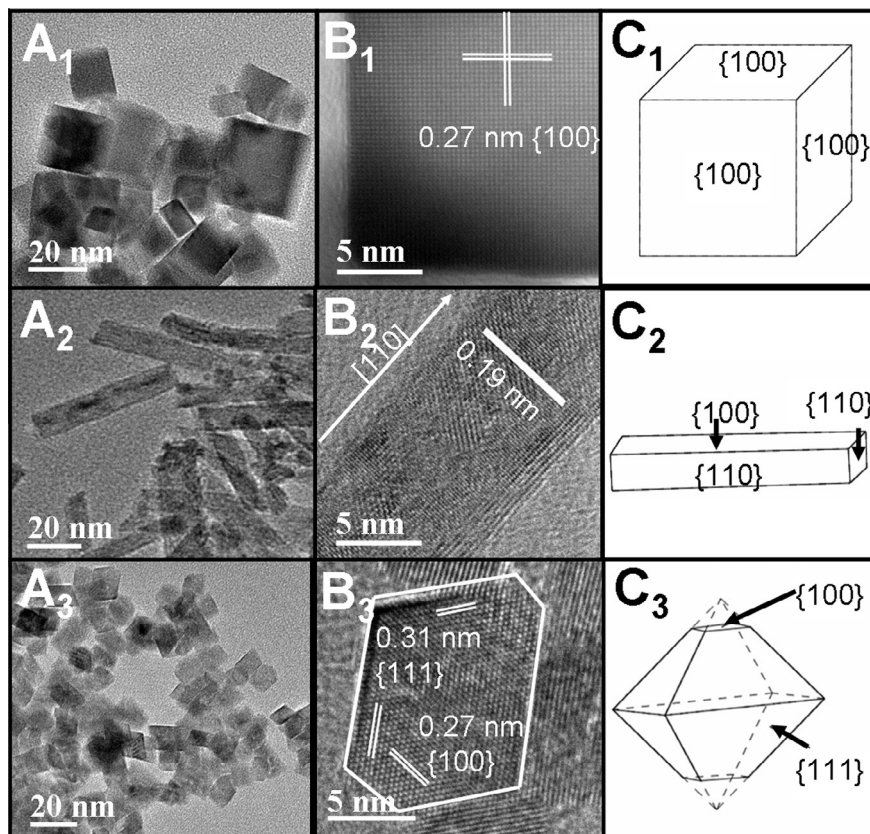


Fig. 1. (A) TEM images, (B) HRTEM images, and (C) schematic illustrations for: (A₁, B₁, C₁) CeO₂-NCs, (A₂, B₂, C₂) CeO₂-NRs, (A₃, B₃, C₃) CeO₂-NPs.

are of pure cubic phase (fluorite structure, JCPDS 34-0394, space group *Fm-3m*) [38]. The peak width at half height of CeO₂-NCs reflections is slightly narrower than that of CeO₂-NRs and CeO₂-NPs, implying a relatively larger particle size compared with the latter two samples. After the introduction of ruthenium supported on CeO₂, the resulting Ru(3%)/CeO₂ samples show close Ru loadings (determined by ICP-AES measurements) in despite of some weight loss compared with the feed intake (Table 1). However, no distinct XRD reflections of Ru species can be observed for all the three samples (Fig. 2d–f), indicating a high dispersion of Ru species in these Ru(3%)/CeO₂ samples.

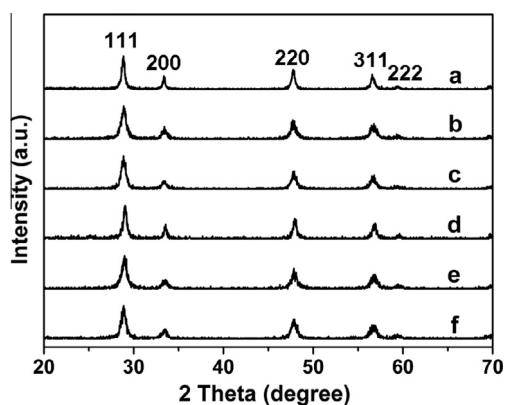


Fig. 2. XRD patterns of: (a) CeO₂-NCs, (b) CeO₂-NRs, (c) CeO₂-NPs, (d) Ru(3%)/CeO₂-NCs, (e) Ru(3%)/CeO₂-NRs, (f) Ru(3%)/CeO₂-NPs.

TEM and HRTEM measurements were further carried out to give structural information for the supported Ru/CeO₂ catalysts (Fig. 3). It can be seen that the three CeO₂ supports inherit their original morphology after the loading of Ru. For the sample of Ru(3%)/CeO₂-NCs, nanocrystals with the average particle diameter of 3.2 nm (Fig. S2 and Table S1) are observed on the surface of CeO₂-NCs (Fig. 3A). This is attributed to the supported metal Ru species based on the EDS spectra (Fig. S3) as well as the corresponding lattice spacings of 0.204 nm and 0.214 nm indexed to the {101} and {002} planes of hexagonal close-packed (hcp) Ru (Fig. 3B). In the cases of Ru(3%)/CeO₂-NRs and Ru(3%)/CeO₂-NPs, TEM images show relatively smaller particle diameter of Ru with 1.7 nm and 2.0 nm, respectively (Fig. 3, Fig. S2). The H₂-TPD measurement was further performed to obtain the specific Ru dispersity (Table 1), and the results show that Ru(3%)/CeO₂-NRs and Ru(3%)/CeO₂-NPs display much higher Ru dispersity (69.9% and 54.4%, respectively) than that of Ru(3%)/CeO₂-NCs (35.0%). The

Table 1
Structural parameters for various catalysts.

Sample	S _{BET} (m ² g ⁻¹)	Ru ^a (wt%)	Ru dispersity ^b (%)	OSC _{surface-e} (μmol O g ⁻¹)	OSC _{surface-t} (μmol O g ⁻¹)
CeO ₂ -NCs	36.2	–	–	11 ± 3	205
CeO ₂ -NRs	61.8	–	–	16 ± 5	423
CeO ₂ -NPs	67.6	–	–	13 ± 3	442
Ru(3%)/CeO ₂ -NCs	34.2	2.3 ± 0.2	35.0 ± 3.7	171 ± 5	194
Ru(3%)/CeO ₂ -NRs	60.3	2.5 ± 0.2	69.9 ± 4.1	43 ± 4	413
Ru(3%)/CeO ₂ -NPs	64.6	2.5 ± 0.1	54.4 ± 3.5	79 ± 4	422

^a Values determined by ICP.

^b Values calculated based on the H₂-TPD results.

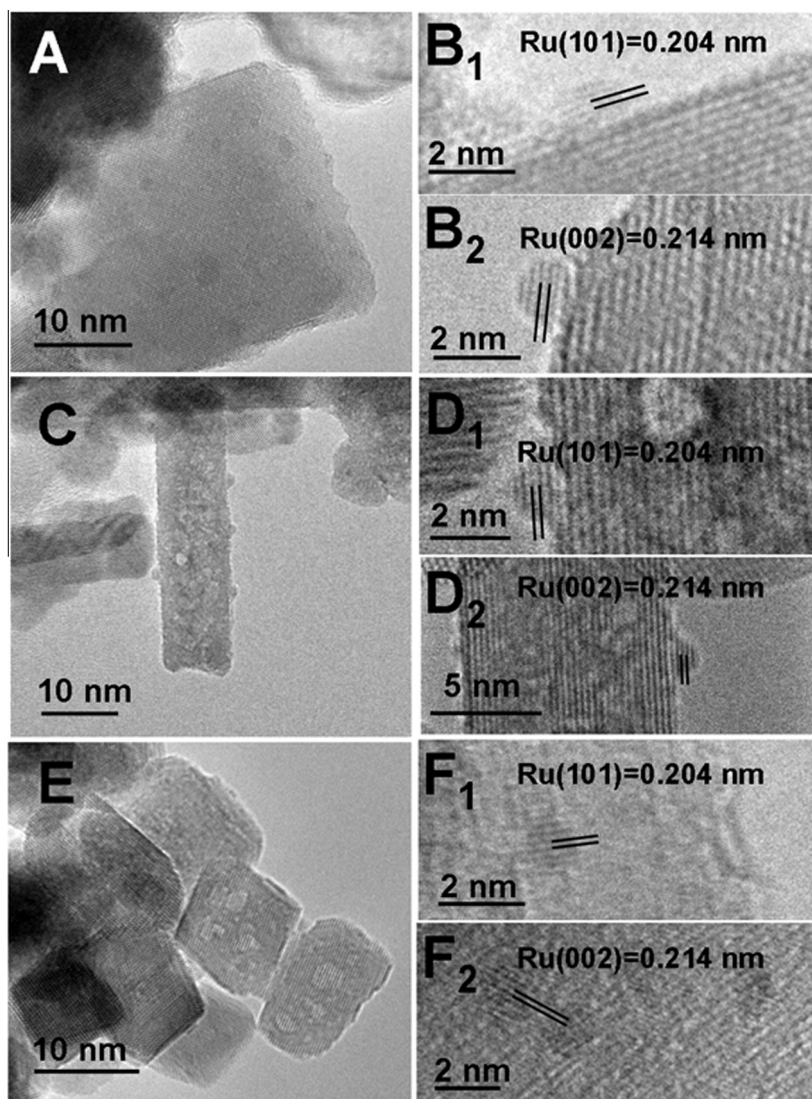


Fig. 3. TEM and HRTEM images of: (A, B) Ru(3%)/CeO₂-NCs, (C, D) Ru(3%)/CeO₂-NRs, (E, F) Ru(3%)/CeO₂-NPs.

average particle diameter ($d_{\text{dispersion}}$) based on metal dispersion was calculated as hemispherical particles (see details in Section 2.4), and the results are shown in Table S1. The average particle diameter of Ru in Ru(3%)/CeO₂-NCs (3.7 nm) is much larger than that in Ru(3%)/CeO₂-NRs (1.8 nm) and Ru(3%)/CeO₂-NPs (2.3 nm), which is consistent with the trend observed by TEM. The coordination structure of Ru atom in these samples was further characterized by extended X-ray absorption fine structure (EXAFS) spectroscopy (Fig. S4). The fitting parameters (Table 2) show that all the Ru–Ru coordination numbers in the three

Table 2
EXAFS fitting parameters of Ru foil and the three Ru(3%)/CeO₂ samples.

Samples	N^a	$R^b(\text{\AA})$	$\sigma^2 \times 10^{-3c}$ (A ²)	ΔE_0^d (eV)
Ru foil	12.0	2.64	3.6	4.40
Ru(3%)/CeO ₂ -NCs	10.5	2.64	3.3	3.98
Ru(3%)/CeO ₂ -NRs	6.5	2.64	3.1	3.43
Ru(3%)/CeO ₂ -NPs	8.1	2.64	3.2	4.06

^a Coordination number.

^b Bonding distance.

^c Debye–Waller factor.

^d Inner potential shift.

supported Ru samples are lower than that of Ru foil (12) and decrease in the following order: Ru(3%)/CeO₂-NCs (10.5) > Ru(3%)/CeO₂-NPs (8.1) > Ru(3%)/CeO₂-NRs (6.5). This indicates that Ru(3%)/CeO₂-NRs and Ru(3%)/CeO₂-NPs possess a higher unsaturation level of Ru–Ru coordination than Ru(3%)/CeO₂-NCs. Karim et al. [39] and Frenkel et al. [40] reported detailed investigations on the EXAFS coordination number vs. particle diameter of metal species (Fig. S5). Based on Karim and Frenkel's calculation models, we estimated the average particle diameter of Ru to be ~4.0 nm (Ru(3%)/CeO₂-NCs), ~1.0 nm (Ru(3%)/CeO₂-NRs), and ~1.6 nm (Ru(3%)/CeO₂-NPs), respectively (Table S1). The results of TEM, H₂-TPD, and EXAFS reveal that the average particle size of Ru in Ru(3%)/CeO₂-NCs is larger than that in Ru(3%)/CeO₂-NRs and Ru(3%)/CeO₂-NPs.

3.2. Metal–support interaction between Ru and CeO₂ with various morphologies

Previous reports have revealed the close relationship between the metal–support interaction and the concentration of oxygen vacancy [23–25,41–43]. In order to give a further insight into the metal–support interaction in these Ru(3%)/CeO₂ samples, TPR

and XPS measurements were performed. For the H₂-TPR profiles (Fig. 4), three main peaks are observed for the three RuO₂(3%)/CeO₂ samples. The first two peaks (at 92–99 °C and 143–148 °C) can be assigned to the reduction of RuO₂, while the peak at 815–835 °C is due to the reduction of bulk CeO₂ [44,45]. The presence of the two peaks below 200 °C indicates that RuO₂ exists in two different states: The RuO₂ species interacting strongly with ceria surface would be reduced at a lower temperature, while the one that weakly interacts with the support is reduced at a relatively higher temperature. For the sample of RuO₂(3%)/CeO₂-NCs (Fig. 4a), the area of the low-temperature (99 °C) peak accounts for 47.1% of the total area below 200 °C. In the cases of RuO₂(3%)/CeO₂-NRs and RuO₂(3%)/CeO₂-NPs however, the low-temperature peak accounts for 70.5% and 67.2%, respectively, which is much larger than that in RuO₂(3%)/CeO₂-NCs.

The enlarged TPR profiles of these three samples are shown in the inset of Fig. 4. Two peaks at 254 and 340 °C are evident for RuO₂/CeO₂-NCs, while only one peak is observed for RuO₂(3%)/CeO₂-NRs (337 °C) and RuO₂(3%)/CeO₂-NPs (368 °C), respectively. These weak peaks can be assigned to the reduction of surface cerium oxide which appears at ~480 °C for pure CeO₂ (Fig. S6). These reduction peaks for the surface CeO₂ of RuO₂(3%)/CeO₂ samples are far below that of the pure CeO₂. While for the reduction peaks of RuO₂ below 200 °C, a quantitative estimation of the H₂ consumption greatly exceeds the theoretically calculated amount. This implies that a large amount of H₂ consumed below 200 °C is used to remove the readily available surface oxygen of CeO₂. The reduction degree of CeO₂ in these samples is calculated and listed in Table S2. For the sample of RuO₂(3%)/CeO₂-NCs, a stoichiometry of CeO_{1.90} is obtained at 200 °C, with a slight decrease to CeO_{1.89} at 600 °C. In contrast, for RuO₂(3%)/CeO₂-NRs and RuO₂(3%)/CeO₂-NPs, the reduction below 200 °C induces CeO_{1.95} and CeO_{1.97}, which further changes to CeO_{1.93} and CeO_{1.96} at 600 °C, respectively. The results indicate that more surface oxygen of CeO₂ is removed below 200 °C for the formation of abundant oxygen vacancies in the sample of Ru(3%)/CeO₂-NCs, which may due to the hydrogen spillover mechanism reported previously [46–49].

XPS was employed to probe the chemical states of ruthenium species in Ru(3%)/CeO₂ samples. For the sample of Ru(3%)/CeO₂-NCs (Fig. 5a), a peak at 280.1 eV corresponds to the Ru 3d_{5/2} of Ru NPs. In the cases of Ru(3%)/CeO₂-NRs (Fig. 5b) and Ru(3%)/CeO₂-NPs (Fig. 5c), the peak at 280.1 eV for Ru 3d_{5/2} becomes much weaker; an additional peak at 281.1 eV is observed (~52.0% and 34.0% of the total Ru, respectively), which can be attributed to Ru_n⁺ most likely existing at the interface between Ru and CeO₂ [49]. The presence of Ru_n⁺ indicates a metal–support interaction with the electron transfer from Ru to support in

Ru(3%)/CeO₂-NRs and Ru(3%)/CeO₂-NPs, which would significantly influence the concentration/type of oxygen vacancies and the resulting catalytic performances. This will be further discussed in the next section.

3.3. Concentration/type of the oxygen vacancies

Oxygen vacancy is an essential defect that often serves as the reactive site on the surface of metal oxides. In Ru/CeO₂ catalysts, the oxygen vacancy may act as an important cooperative site in addition to metal active sites. The TPR of Ru(3%)/CeO₂ and their reduction degree of the support (Fig. 4 and Table S2) have shown that the formation of oxygen vacancy is clearly morphology/facet-dependent. Raman, OSC test, and positron annihilation spectroscopy were employed to further confirm the concentration/type of oxygen vacancies and their formation mechanism. Fig. 6 shows Raman spectra of CeO₂, RuO₂(3%)/CeO₂, and Ru(3%)/CeO₂ excited at 514.5 nm laser. All the three CeO₂ supports (NCs, NRs, and NPs) exhibit a strong peak at 462 cm⁻¹, corresponding to the vibration model of octahedral local symmetry around CeO₂ lattice (F_{2g}) (Fig. 6A). The other two weak peaks at 598 and 1174 cm⁻¹ are indicative of the presence of defect-induced (D) modes and second-order longitudinal modes of cubic CeO₂ fluoride phase, respectively [23–25]. The relative intensity ratio of I_D/I_{F2g} implies the concentration of defect sites on CeO₂, which decreases in the following order: CeO₂-NRs (0.04) > CeO₂-NCs (0.03) > CeO₂-NPs (0.01) (Fig. 6D, curve a). After the loading of Ru and calcination, the Raman spectra for RuO₂/CeO₂ samples are more complicated (Fig. 6B). Besides the peaks of CeO₂, two peaks at 690 and 960 cm⁻¹ are observed, which can be assigned to Ru–O–Ce bond resulting from the metal–support interaction [50]. For the samples of RuO₂(3%)/CeO₂, the I_D/I_{F2g} ratio has no obvious change (Fig. 6D, curve b). However, in the case of Ru(3%)/CeO₂ samples reduced in H₂ atmosphere, a significant increase occurs for the I_D/I_{F2g} value, indicating the vital role of reduction process in the formation of oxygen vacancies (Fig. 6C). The largest I_D/I_{F2g} value is obtained for Ru(3%)/CeO₂-NCs (0.70), much superior to Ru(3%)/CeO₂-NRs (0.17) and Ru(3%)/CeO₂-NPs (0.13) (Fig. 6D, curve c). For comparison, the I_D/I_{F2g} value of pure CeO₂ after reduction in H₂ atmosphere only slightly increases to 0.04–0.06 (Fig. S7). The results show that more oxygen vacancies are formed in the Ru(3%)/CeO₂-NCs sample than the other two systems, in accordance with the TPR results.

To further understand the role of Ru species in the formation of oxygen vacancies, RuO₂/CeO₂-NCs and Ru/CeO₂-NCs samples with various Ru loading were also studied with Raman spectra (Fig. S8). For RuO₂/CeO₂-NCs samples (Fig. S8A), the intensity of the two

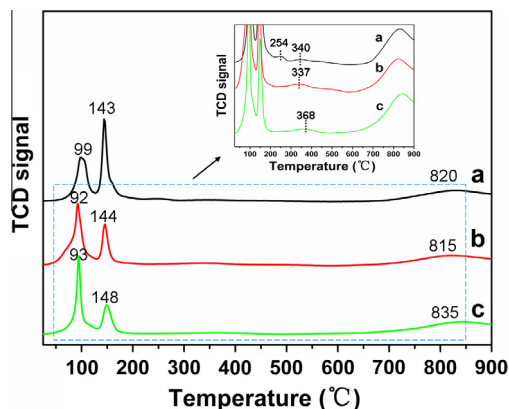


Fig. 4. H₂-TPR profiles of: (a) RuO₂(3%)/CeO₂-NCs, (b) RuO₂(3%)/CeO₂-NRs, (c) RuO₂(3%)/CeO₂-NPs.

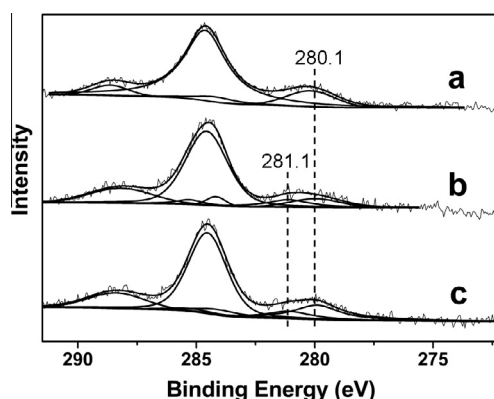


Fig. 5. XPS profiles of (a) Ru(3%)/CeO₂-NCs, (b) Ru(3%)/CeO₂-NRs, (c) Ru(3%)/CeO₂-NPs.

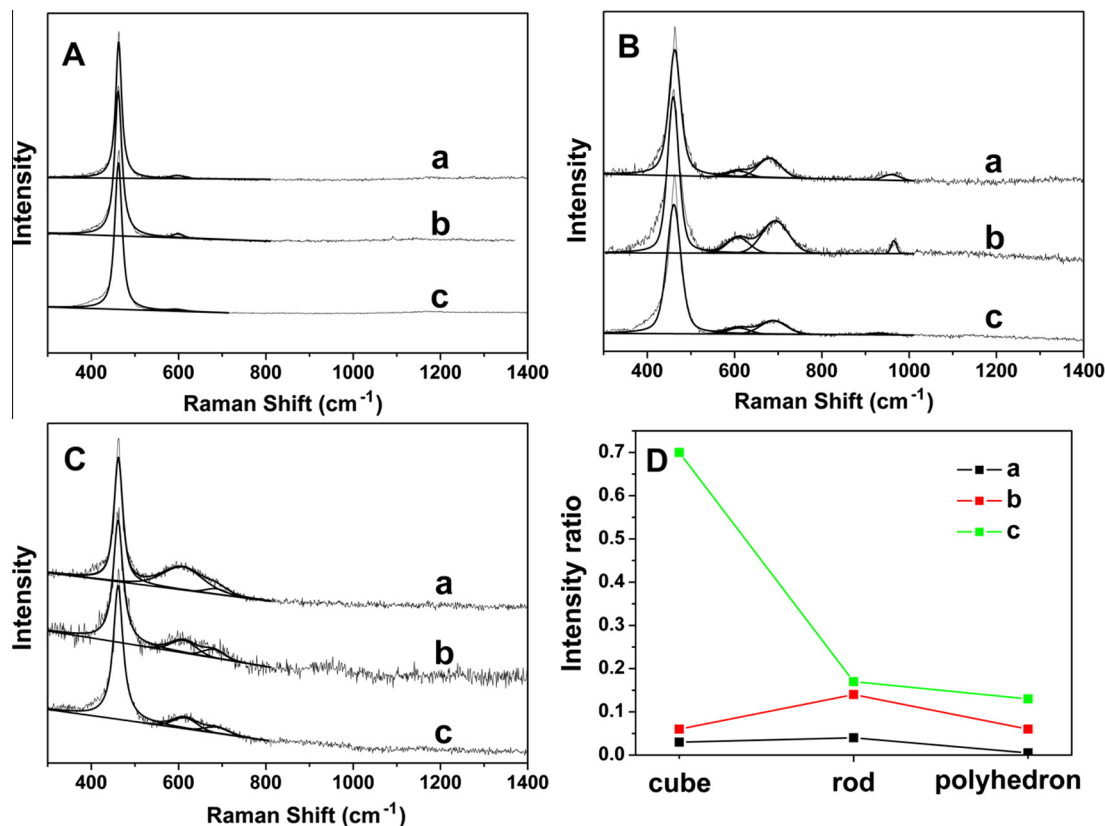


Fig. 6. Visible Raman spectra of (A) CeO₂, (B) RuO₂(3%)/CeO₂, (C) Ru(3%)/CeO₂ samples: (a) CeO₂-NCs, (b) CeO₂-NRs, (c) CeO₂-NPs. (D) The corresponding I_D/I_{F2g} values: (a) CeO₂, (b) RuO₂(3%)/CeO₂, (c) Ru(3%)/CeO₂.

bands at 690 and 963 cm⁻¹ increases along with the increase in Ru loading from 1% to 13%, indicating the enhanced Ru–O–Ce bonding. At the same time, the peak assigned to defect-induced (D) modes has no obvious change, further confirming the oxygen vacancies are not formed in the Ru loading and calcination process. For Ru/CeO₂-NCs samples (Fig. S8B), the I_D/I_{F2g} value significantly increases from Ru(1%)/CeO₂-NCs (0.38) to Ru(13%)/CeO₂-NCs (1.21), indicating the gradually increased oxygen vacancies in the reduction process. With the enhancement of Ru loading (from 0.8% to 9.2%), the particle size of Ru increases (from 3.2 nm to 4.3 nm), while the BET area (from 35.3 m² g⁻¹ to 30.6 m² g⁻¹) and metal dispersion (from 39.5% to 29.6%) decrease gradually (Table S3), due to the aggregation of Ru.

OSC tests were employed to determine the concentration of oxygen vacancies in the CeO₂ surface quantitatively (shown in Table 1). The catalyst was reduced at 400 °C followed by the uptake of O₂ at room temperature (25 °C), and the value of O₂ uptake was corrected by OSC_{metal}. Compared with the pure CeO₂ (11, 16, 13 μmol O g⁻¹ for CeO₂-NCs, CeO₂-NRs, and CeO₂-NPs, respectively), the OSC_{surface-e} values of Ru(3%)/CeO₂ catalysts show a marked increase. The Ru(3%)/CeO₂-NCs sample gives an OSC_{support-e} value of 171 μmol O g⁻¹, much larger than Ru(3%)/CeO₂-NRs (43 μmol O g⁻¹) and Ru(3%)/CeO₂-NPs (79 μmol O g⁻¹), which coincides with the Raman results. The theoretical maximum of surface oxygen vacancy concentration (OSC_{surface-t}) was further calculated according to the crystal institutions (Table 4). The OSC_{surface-t} values are 194 μmol O g⁻¹, 413 μmol O g⁻¹, and 422 μmol O g⁻¹ for Ru(3%)/CeO₂-NCs, Ru(3%)/CeO₂-NRs, and Ru(3%)/CeO₂-NPs, respectively. The determined concentration of surface oxygen vacancy is lower than that of the theoretical maximum, indicating that Ce⁴⁺ and Ce³⁺ coexist in the surface of CeO₂.

Positron annihilation spectroscopy (PAS) is a powerful tool to study defects in solids, which can provide information about the size, type, and relative density of various defects [26]. Table 3 lists the positron lifetime components (τ_1 , τ_2 , and τ_3) and corresponding relative intensities (I_1 , I_2 , and I_3) for the Ru/CeO₂ samples and pristine CeO₂. The shortest one (τ_1) is attributed to small neutral Ce³⁺-oxygen vacancy associates and mono-vacancies. The intermediate component τ_2 arises from larger-size oxygen vacancy clusters (i.e., dimmers, trimmers, or larger), resulting from interaction between the small neutral Ce³⁺-oxygen vacancy associates. The longest-lived component (τ_3) is probably caused by the annihilation of orthopositronium atoms formed in the large voids present in the material. Besides the lifetime of positron, the I_2/I_1 ratio gives more information on the relative concentration proportion of oxygen vacancy clusters (large size) to neutral vacancy associates (small size) in this material. After the loading of Ru, the I_2/I_1 ratio increases from CeO₂-NCs (0.50) to Ru(3%)/CeO₂-NCs (0.88). However, for the other two samples, the ratio decreases from CeO₂-NRs (0.61) to Ru(3%)/CeO₂-NRs (0.55) and from CeO₂-NPs (0.55) to Ru(3%)/CeO₂-NPs (0.51). According to the previous report, the migration of oxygen in ceria and ceria-based

Table 3
Positron lifetimes and relative intensities.

Sample	τ_1 (ps)	τ_2 (ps)	τ_3 (ns)	I_1 (%)	I_2 (%)	I_3 (%)	I_2/I_1
CeO ₂ -NCs	173.4	372.4	2.40	64.2	32.4	3.4	0.50
Ru(3%)/CeO ₂ -NCs	185.6	375.2	2.46	51.7	45.5	2.8	0.88
CeO ₂ -NRs	179.5	369.2	2.51	60.1	36.7	3.2	0.61
Ru(3%)/CeO ₂ -NRs	196.7	410.8	2.50	62.7	34.3	3.0	0.55
CeO ₂ -NPs	180.5	378.4	2.30	61.6	34.1	4.3	0.55
Ru(3%)/CeO ₂ -NPs	200.4	407.8	2.52	63.5	32.5	4.0	0.51

materials takes place *via* a vacancy hopping mechanism; oxygen vacancy clusters with more than two vacancies are favorable for the migration of oxygen. If the diffusion of oxygen anions is sufficiently fast, a continuous supply of oxygen from the bulk to the surface would guarantee an enhanced reducibility.

The shape-dependent concentration and structure of oxygen vacancies in CeO₂ nanocrystals have been reported previously [23–25]. Most early studies show that the vacancy formation energy on different crystal planes of CeO₂ plays the decisive role; recent reports are mainly focused on the metal–support interaction and the chemophysical state of supported metal. However, how these factors influence the formation process of oxygen vacancy is still unclear. In this work, we found that the formation of oxygen vacancy mainly occurs in the reduction process. According to the chemical state of Ru at the metal–support interface shown by XPS, we deduce that the assistance of metal Ru (hydrogen dissociation) at the metal–support interface plays a major role in the morphology/facet-dependent oxygen vacancy. The Ru species in the sample of Ru(3%)/CeO₂-NCs (Ru⁰ with large particle size and low unsaturation) enhances the reduction degree of CeO₂-NCs, resulting in abundant surface oxygen vacancies, in comparison with Ru(3%)/CeO₂-NRs and Ru(3%)/CeO₂-NPs.

3.4. Evaluation of the catalytic behavior

To establish the structure–activity relationship, the reaction rates were evaluated at a low reaction temperature (150 °C), low CO₂ conversion (<10%, Fig. S1) and high CO₂ weight hourly space velocity (WHSV: 360 mL g_{cat}⁻¹ h⁻¹), so as to minimize the effect of mass transport and water inhibition. The reaction rate of Ru(3%)/CeO₂-NCs is 4.85 × 10⁻⁸ mol g_{cat}⁻¹ s⁻¹, which is much higher than that of Ru(3%)/CeO₂-NRs and Ru/CeO₂-NPs (1.15 × 10⁻⁸ mol g_{cat}⁻¹ s⁻¹ and 2.30 × 10⁻⁸ mol g_{cat}⁻¹ s⁻¹, respectively). The apparent activation energies (*E_a*) for these Ru(3%)/CeO₂ catalysts are calculated from the Arrhenius plots (Fig. 7), which are listed in Table 4. The *E_a* values of Ru(3%)/CeO₂-NCs (72.9 ± 4.2 kJ mol⁻¹),

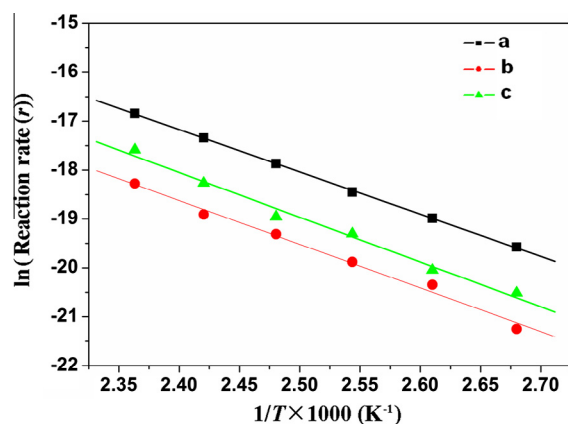


Fig. 7. Ln(CH₄ formation rate) vs. reciprocal of reaction temperature over: (a) Ru(3%)/CeO₂-NCs, (b) Ru(3%)/CeO₂-NRs, and (c) Ru(3%)/CeO₂-NPs measured from 100 to 150 °C in CO₂ methanation.

Ru(3%)/CeO₂-NRs (76.4 ± 2.7 kJ mol⁻¹), and Ru(3%)/CeO₂-NPs (76.1 ± 5.1 kJ mol⁻¹) do not show obvious difference, indicating that these catalysts provide the same active site and obey the same reaction mechanism. It should be noted that the TOF values with respect to the exposed Ru atom (TOF_{Ru}) are significantly different for the three catalysts (6.06 × 10⁻⁴ s⁻¹, 6.61 × 10⁻⁵ s⁻¹, 1.72 × 10⁻⁴ s⁻¹ for Ru(3%)/CeO₂-NCs, Ru(3%)/CeO₂-NRs, and Ru(3%)/CeO₂-NPs, respectively), while the TOF values with respect to surface oxygen vacancy (TOF_{oxygen vacancy}) are rather close (2.84 × 10⁻⁴ s⁻¹, 2.67 × 10⁻⁴ s⁻¹, 2.91 × 10⁻⁴ s⁻¹ for Ru(3%)/CeO₂-NCs, Ru(3%)/CeO₂-NRs, and Ru(3%)/CeO₂-NPs, respectively). This indicates that not the supported Ru but the surface oxygen vacancy is the active site for the rate-determining step in this reaction. Several control samples with Al₂O₃, MgO, and SiO₂ supports are prepared by the same precipitation deposition method described in this work, and the basic characterizations are listed in Table S4. The catalytic reaction rate of Ru(3%)/CeO₂-NCs is superior to these samples under the same reaction conditions (Table S4). Although CO₂ is very chemically stable, oxygen vacancy can catalyze its reduction at appreciable rates, which has been confirmed previously based on experimental and DFT study over pure CeO₂ [51,52]. For metal/CeO₂ systems, it has been reported that the oxygen vacancies in reduced ceria are the catalytic active sites for CO₂ adsorption and activation, while the supported metal provides a reactive H-species through H₂ activation [35,53,54]. Based on previous reports [33,37] and the results in this work, it is concluded that oxygen vacancy on the CeO₂ surface serves as the active site for CO₂ methanation, while Ru provides H-species for hydrogenation reaction and recycling of oxygen vacancy. According to the results of OSC measurements, a linear relationship between the catalytic rate and surface oxygen vacancy concentration (OSC_{surface-e}) is obtained, which almost passes through the origin (Fig. 8). This demonstrates the quantitative structure–property correlation between catalytic reaction rate and oxygen vacancy in this reaction. The sample of Ru(3%)/CeO₂-NCs with the most abundant oxygen vacancies exhibits the highest catalytic reaction rate.

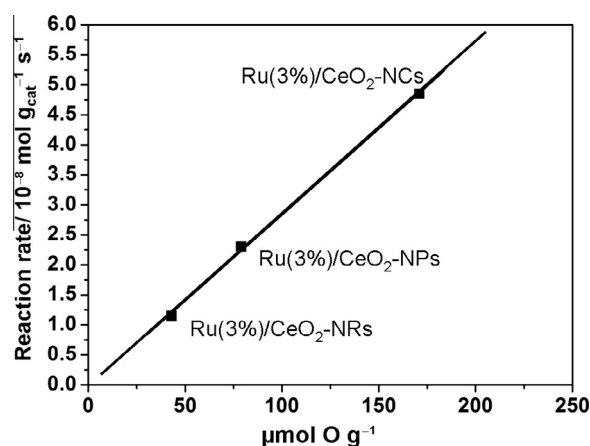


Fig. 8. Reaction rate at 150 °C as a function of the concentration of surface oxygen vacancy (OSC_{support-e}).

Table 4
Catalytic performances for various catalysts.

Sample	Reaction rate ^a (mol g _{cat} ⁻¹ s ⁻¹)	TOF _{Ru} ^b (s ⁻¹)	TOF _{oxygen vacancy} ^b (s ⁻¹)	<i>E_a</i> (kJ mol ⁻¹)
Ru(3%)/CeO ₂ -NCs	(4.85 ± 0.23) × 10 ⁻⁸	(6.06 ± 0.28) × 10 ⁻⁴	(2.84 ± 0.42) × 10 ⁻⁴	72.9 ± 4.2
Ru(3%)/CeO ₂ -NRs	(1.15 ± 0.11) × 10 ⁻⁸	(6.61 ± 0.91) × 10 ⁻⁵	(2.67 ± 0.25) × 10 ⁻⁴	76.4 ± 2.7
Ru(3%)/CeO ₂ -NPs	(2.30 ± 0.36) × 10 ⁻⁸	(1.72 ± 0.27) × 10 ⁻⁴	(2.91 ± 0.37) × 10 ⁻⁴	76.1 ± 5.1

^a The reaction rate (*r*) was defined as the mole number of CH₄ produced per gram of catalyst per second.

^b The TOF values were calculated at 150 °C. All the catalytic performances were tested for 5 times.

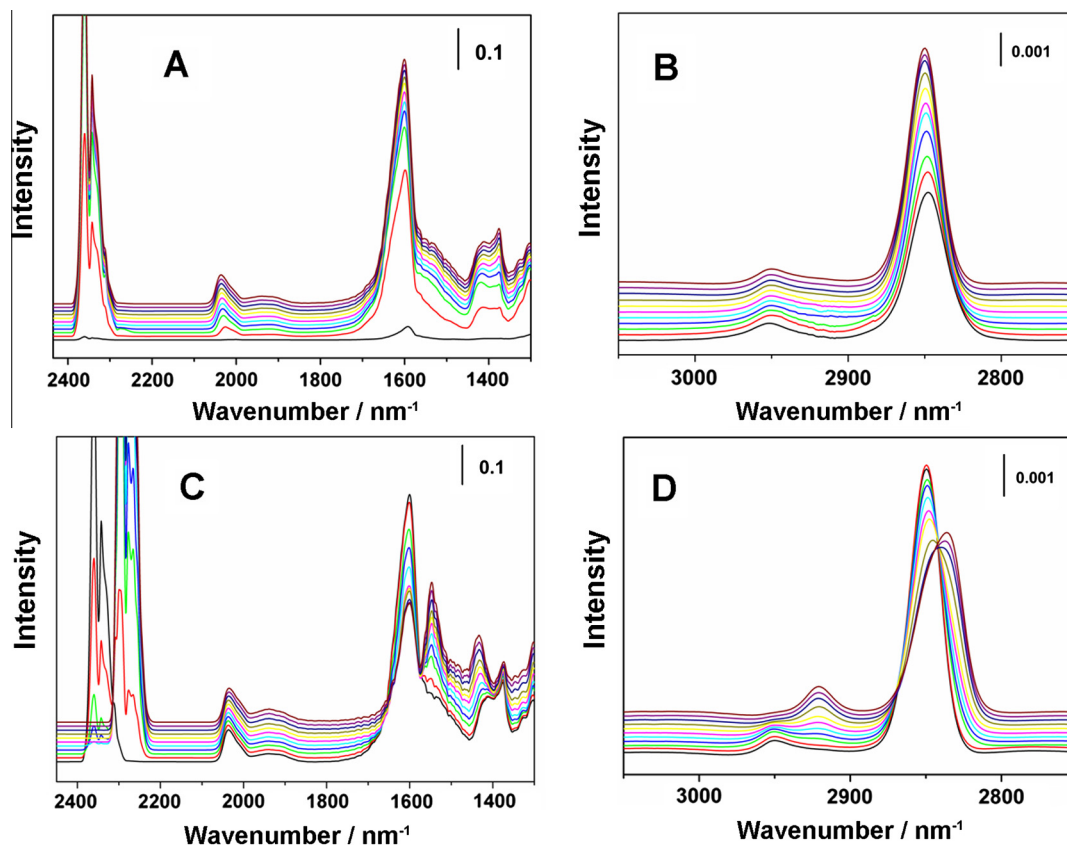


Fig. 9. (A, B) DRIFT spectra recorded at 150 °C during 90 min over the Ru(3%)/CeO₂-NCs catalyst with ¹²CO₂ as reaction gas; (C, D) subsequent reaction during 45 min by introducing ¹³CO₂ as reaction gas. From bottom to top: (A, B) 0, 0.5, 2, 5, 10, 15, 20, 30, 50, 70, 90 min; (C, D) 0, 0.5, 1, 2, 4, 6, 10, 15, 20, 30, 45 min.

Fig. S9 shows the Koros–Nowak (KN) criterion plot of the CH₄ formation rate per gram of Ru/CeO₂-NCs catalysts, which exhibits a linear increase along with the Ru loading from Ru(1%)/CeO₂-NCs to Ru(13%)/CeO₂-NCs at 150 °C. This indicates that the catalytic reaction over these catalysts obeys the KN criterion, and the reaction rate is not influenced by the mass transport.

To further investigate the role of oxygen vacancy in CO₂ activation, the catalytic reaction mechanism over Ru(3%)/CeO₂-NCs catalyst was studied by steady-state isotope transient kinetic analysis (SSITKA)-type *in-situ* DRIFT infrared spectroscopy. After 90 min of reaction at 150 °C, CO₂ was replaced by the isotopic gas (¹³CO₂) for another 45 min of reaction. By correlating the build-up/decay of various surface species including CO, formate, and carbonate, detailed information on the catalytic reaction mechanism can be obtained. Fig. 9A and B show the *in situ* DRIFT infrared spectra of Ru(3%)/CeO₂-NCs at 150 °C over 90 min. Once the reaction gas mixture is introduced, characteristic signals of the gas phase CO₂ (2361 and 2343 cm⁻¹), CO_{ad} (2036 and 1940 cm⁻¹), formate (1602 and 1376 cm⁻¹), carbonate (1416 cm⁻¹), and methyl group (2954 and 2846 cm⁻¹) are observed immediately. These bands are almost saturated over 90 min. The band at 3016 cm⁻¹ attributed to methane is not detected, probably due to the weak adsorption on the catalyst surface. When CO₂ was replaced from ¹²CO₂ by ¹³CO₂, significant changes occur in the DRIFT spectra (Fig. 9C and D). The characteristic bands of ¹²CO_{2,gas} diminish gradually, while new bands ascribed to ¹³CO_{2,gas} (2295, 2278, and 2267 cm⁻¹) are found, confirming the switchover of isotopic CO₂ gas. The characteristic bands of formate (1602 cm⁻¹) and methyl group (2954 and 2846 cm⁻¹) display a similar trend as CO₂. These bands decrease, while the corresponding new bands attributed to ¹³C-formate (1549 cm⁻¹) and ¹³C-methyl group (2922 and

2833 cm⁻¹) grow steadily. This indicates that formate and methyl group are intermediates in the main reaction path. The methyl group generally belongs to methyl alcohol and CH_x chains. Owing to the inactivity property of CH_x chains under this catalytic condition [55], methyl alcohol is very likely to be the intermediate. At the same time, the characteristic bands of CO_{ad} and carbonate do not show obvious change over the reaction period of 45 min, indicating that these species are side products other than reaction intermediates. The CO₂ hydrogenation reaction path with the assistance of oxygen vacancy has already been proved to undergo formate and methyl alcohol by Ye et al. [56] by using DFT calculation, and the results in this work coincide with the previous report.

4. Conclusions

In summary, we have fabricated a series of Ru/CeO₂ catalysts with tunable CeO₂ morphology/facet and Ru loading, which exhibit significantly support-morphology-dependent catalytic activity toward CO₂ methanation. The Ru(3%)/CeO₂-NCs catalyst shows an extraordinarily high catalytic rate per gram of catalyst over the Ru(3%)/CeO₂-NCs catalyst (reaction rate: 4.85×10^{-8} mol g_{cat}⁻¹ s⁻¹; selectivity: 99%; 150 °C). The results of Raman spectra and OSC test demonstrate that oxygen vacancies with a high concentration are produced at the surface of Ru(3%)/CeO₂-NCs during the reduction process, owing to the metal Ru⁰-promoted effect on the formation of oxygen vacancy. In addition, *in situ* infrared spectroscopy measurements verify the presence of oxygen vacancy facilitates the activation and conversion of inert CO₂, accounting for the highest reaction rate at a low temperature. This work not only provides a

facile method for the preparation of highly efficient Ru/CeO₂ catalysts by modulating the exposed facet of support, but also offers a fundamental understanding of the key role of concentration of oxygen vacancies in the hydrogenation reactions. It is expected that this strategy can be extended to the fabrication of other supported metal catalysts with significantly enhanced behavior in heterogeneous catalysis.

Acknowledgments

This work was supported by the 973 Program (Grant No.: 2011CBA00504), the National Natural Science Foundation of China (NSFC), the Scientific Fund from Beijing Municipal Commission of Education, and the Beijing Natural Science Foundation (2132043). M. Wei particularly appreciates the financial aid from the China National Funds for Distinguished Young Scientists of the NSFC. We thank for the support of BSRF (Beijing Synchrotron Radiation Facility) during the XAFS and PAS measurements.

We gratefully acknowledge Dr. Bin Wang at SINOPEC Beijing Research Institute of Chemical Industry for assistance to perform *in-situ* DRIFT infrared spectroscopy.

Appendix A. Supplementary material

Supplementary data associated with this article can be found, in the online version, at <http://dx.doi.org/10.1016/j.jcat.2015.05.014>.

References

- [1] A. Trovarelli, *Catal. Rev.* 38 (1996) 439.
- [2] M. Cargnello, V. Doan-Nguyen, T.R. Gordon, R.E. Diaz, E.A. Stach, R.J. Gorte, P. Fornasiero, C.B. Murray, *Science* 341 (2013) 771.
- [3] S. Aranifard, S.C. Ammal, A. Heyden, *J. Catal.* 309 (2014) 314.
- [4] T. Masui, K. Fujiwara, K. Machida, G. Adachi, *Chem. Mater.* 9 (1997) 2197.
- [5] T. Masui, M. Yamamoto, T. Sakata, H. Mori, G. Adachi, *J. Mater. Chem.* 10 (2000) 353.
- [6] E.P. Murray, T. Tsai, S.A. Barnett, *Nature* 400 (1999) 649.
- [7] S. McIntosh, R.J. Gorte, *Chem. Rev.* 104 (2004) 4845.
- [8] N. Izu, W. Shin, N. Murayama, S. Kanzaki, *Sens. Actuators B* 87 (2002) 95.
- [9] J. Guzman, S. Carrettin, A. Corma, *J. Am. Chem. Soc.* 127 (2005) 3286.
- [10] S. Carrettin, P. Concepción, A. Corma, J.M.L. Nieto, V.F. Puntes, *Angew. Chem. Int. Ed.* 43 (2004) 2538.
- [11] Q. Li, Y. Zhang, G. Chen, J. Fan, H. Lan, Y. Yang, *J. Catal.* 273 (2010) 167.
- [12] G. Avgouropoulos, T. Ioannides, H. Matralis, *Appl. Catal. B* 56 (2005) 87.
- [13] J. Ke, J. Xiao, W. Zhu, H. Liu, R. Si, Y. Zhang, C. Yan, *J. Am. Chem. Soc.* 135 (2013) 15191.
- [14] H. Zhang, H. Liu, *J. Energy. Chem.* 22 (2013) 98.
- [15] S. Damyanova, J.M.C. Bueno, *Appl. Catal. A* 253 (2003) 135.
- [16] H. Roh, H.S. Potdar, K. Jun, *Catal. Today* 93 (2004) 39.
- [17] Y.H. Taufiq-Yap, Sudarmo, U. Rashid, Z. Zainal, *Appl. Catal. A* 468 (2013) 359.
- [18] X. Wang, Q. Kang, D. Li, *Appl. Catal. B* 86 (2009) 166.
- [19] Y. Dai, X. Wang, Q. Dai, D. Li, *Appl. Catal. B* 111 (2012) 141.
- [20] P. Gawade, B. Mirkelamoglu, U.S. Ozkan, *J. Phys. Chem. C* 114 (2010) 18173.
- [21] I.I. Soykal, B. Bayram, H. Sohn, P. Gawade, J.T. Miller, U.S. Ozkan, *Appl. Catal. A* 449 (2012) 47.
- [22] Z. Wu, M. Li, S.H. Overbury, *J. Catal.* 285 (2012) 67.
- [23] S. Zhang, M. Li, Q. Hua, L. Zhang, Y. Ma, B. Ye, W. Huang, *J. Catal.* 293 (2012) 195.
- [24] L. Liu, Z. Yao, Y. Deng, F. Gao, B. Liu, L. Dong, *ChemCatChem* 3 (2011) 978.
- [25] X. Du, D. Zhang, L. Shi, R. Gao, J. Zhang, *J. Phys. Chem. C* 116 (2012) 10009.
- [26] X. Liu, K. Zhou, L. Wang, B. Wang, Y. Li, *J. Am. Chem. Soc.* 131 (2009) 3140.
- [27] L. Ma, D. Wang, J. Li, B. Bai, L. Fu, Y. Li, *Appl. Catal. B* 148–149 (2014) 36.
- [28] K.R. Thampai, J. Kiwi, M. Grätzel, *Nature* 327 (1987) 506.
- [29] W. Wang, S. Wang, X. Ma, *J. Gong. Chem. Soc. Rev.* 40 (2011) 3703.
- [30] A.E. Ashley, A.L. Thompson, D. O'Hare, *Angew. Chem. Int. Ed.* 48 (2009) 9839.
- [31] C. Li, S. Zhang, B. Zhang, D. Su, S. He, Y. Zhao, J. Liu, F. Wang, M. Wei, D.G. Evans, X. Duan, *J. Mater. Chem. A* 1 (2013) 2461.
- [32] F. Wang, S. Zhang, C. Li, J. Liu, S. He, Y. Zhao, H. Yan, M. Wei, D.G. Evans, X. Duan, *RSC Adv.* 4 (2014) 10834.
- [33] S. Tada, T. Shimizu, H. Kameyama, T. Haneda, R. Kikuchi, *Int. J. Hydrogen Energy* 37 (2012) 5527.
- [34] A. Karelavic, P. Ruiz, *J. Catal.* 301 (2013) 141.
- [35] M.D. Porosoff, J.G. Chen, *J. Catal.* 301 (2013) 30.
- [36] S. Sharma, Z. Hu, P. Zhang, E.W. McFarland, H. Metiu, *J. Catal.* 278 (2011) 297.
- [37] É. Novák, K. Fodor, T. Szailer, A. Oszkó, A. Erdőhelyi, *Top. Catal.* 20 (2002) 107.
- [38] H. Mai, L. Sun, Y. Zhang, R. Si, W. Wang, H. Zhang, H. Liu, C. Yan, *J. Phys. Chem. B* 109 (2005) 24380.
- [39] A.M. Karim, V. Prasad, G. Mpourmpakis, W.W. Lonergan, A.I. Frenkel, J.G. Chen, D.G. Vlachos, *J. Am. Chem. Soc.* 131 (2009) 12230.
- [40] A.I. Frenkel, C.W. Hills, R.G. Nuzzo, *J. Phys. Chem. B* 105 (2001) 12689.
- [41] R. Si, M. Flytzani-Stephanopoulos, *Angew. Chem. Int. Ed.* 47 (2008) 2884.
- [42] Y. Gao, W. Wang, S. Chang, W. Huang, *ChemCatChem* 5 (2013) 3610.
- [43] A. Ciftci, D. Ligthart, P. Pastorino, E. Hensen, *Appl. Catal. B* 130–131 (2013) 325.
- [44] S. Aouad, E. Abi-Aad, A. Aboukaïs, *Appl. Catal. B* 88 (2009) 249.
- [45] S. Hosokawa, H. Kanai, K. Utani, Y. Taniguchi, Y. Saito, S. Imamura, *Appl. Catal. B* 45 (2003) 181.
- [46] K.A. Pokrovski, A.T. Bell, *J. Catal.* 244 (2006) 43.
- [47] V. Sharma, P.A. Crozier, R. Sharma, J.B. Adams, *Catal. Today* 180 (2012) 2.
- [48] J. Chen, Q. Wu, J. Zhang, J. Zhang, *Fuel* 87 (2008) 2901.
- [49] H.Y. Kim, H.M. Lee, G. Henkelman, *J. Am. Chem. Soc.* 134 (2012) 1560.
- [50] A. Satsuma, M. Yanagihara, J. Ohyama, K. Shimizu, *Catal. Today* 201 (2013) 62.
- [51] N. Laosiripojana, S. Assabumrungrat, *Appl. Catal. B* 60 (2005) 107.
- [52] T. Staudt, Y. Lykhach, N. Tsud, T. Skala, K.C. Prince, V. Matolin, J. Libuda, *J. Catal.* 275 (2010) 181.
- [53] Q. Pan, J. Peng, S. Wang, *S. Wang, Catal. Sci. Technol.* 4 (2014) 502.
- [54] C. Leitenburg, A. Trovarelli, J. Kašpar, *J. Catal.* 166 (1997) 98.
- [55] S. Eckle, H. Anfang, R.J. Behm, *J. Phys. Chem. C* 115 (2011) 1361.
- [56] J. Ye, C. Liu, D. Mei, Q. Ge, *ACS Catal.* 3 (2013) 1296.